New insights on the better focusing of FWI derived images

Bruno Pereira Dias, Pedro Bertussi, André Bulcão, Gustavo Catão Alves (PETROBRAS)

Abstract

Deriving images from velocity models obtained from application of Full Waveform Inversion (FWI) at high frequencies has become a reality in large 3D imaging projects. In several published examples, the FWI images deliver superior quality in comparison with traditional Reverse Time Migration (RTM) and Least-Squares Migration (LSM) images. Widespread arguments to explain this improvement include the fact that FWI utilizes multiples events, compensates for transmission losses, and the iterative procedure correct for illumination issues. We will provide an additional argument: the time shift correction in the FWI adjoint source aids the image focusing, especially in inaccurate velocity models. This is observed in a simple synthetic model (primary only, no transmission losses and absent of illumination issues) and in field data with attenuated multiples.

Introduction

Seismic imaging traditionally consisted of two steps: retrieving a low-resolution velocity model and a high-resolution reflectivity. While the velocity models were obtained by tomographic or wavefield methods, reflectivity used these velocity models as inputs for imaging algorithms, such as Kirchhoff, RTM or LSM methods. With this approach, the ability to generate high-resolution velocity models was considered a computationally expensive and challenging task, which became known in the literature as the intermediate wavenumber gap (Claerbout, 1985; Biondi & Almomin, 2013).

Over the last decade, however, a large effort has been made to make FWI more robust. New objective functions were formulated, such as, the adaptive waveform inversion (Warner and Guasch, 2014), graph-space optimal transport (Métivier et al., 2018), enhanced template matching (Vigh et al., 2019), and the time-shift objective function (Luo & Schuster, 1991; Ma & Hale, 2013), also referred as time-lag FWI (Zhang et al 2018). These new approaches represented a significant evolution in the applicability of FWI and were important to guarantee the FWI convergence in high frequencies, since they were less prone to cycle skipping and amplitude fitting errors between modeled and observed data.

Zhang et al. (2020) realized the value of obtaining the high frequency details in the velocity model and proposed a workflow to convert velocity in impedance contrasts or reflectivity. This transforms velocities into "images", which are useful for direct interpretation. More interestingly, the comparison of these images with standard RTM and LSM images revealed that the FWI images were superior in quality and focusing, even in challenging scenarios such as sub-salt imaging in the GoM (Zhang et al. 2020). They accredit this improvement to the fact that FWI is a data-fitting procedure of the full wavefield, which is not restricted to primary reflections. FWI utilizes refractions, diving waves, and multiples events. It also compensates for transmission losses, and the iterative procedure corrects for illumination issues. These arguments are also invoked in (Wei et al, 2021; Huang et al., 2021; and Zhang et al, 2023).

In this work, using synthetic and field data examples we complement the list of reasonings: the time shift correction in the FWI adjoint source aids the image focusing, when propagated in velocity models with residual kinematic errors.

Method

Consider the FWI with time-shift objective function, χ,

$$\chi(m) = \frac{1}{2}\sum_{s,r}\Delta\tau(x_s, x_r)^2, \qquad (1)$$

where m, s, r are the model, source, and receiver position, respectively. Here, $\Delta\tau$ is the measured time shift between observed and modeled data. Zhang et al. (2018) augmented Eq. (1) with a cross-correlation weight to favor good quality measurements in the inversion. This additional term helps to obtain satisfactory results in field applications.

Using the concept of connective function, Luo and Schuster (1991) derived the adjoint source associated with Eq. (1),

$$f^+ = \sum_{s,r}\Delta\tau\frac{\partial}{\partial t}d(t + \Delta\tau). \qquad (2)$$

where $d(t + \Delta\tau)$ is the observed data warped to the measure times of the modeled data $u(t)$. A complementary deduction of the Eq. (2) is provided (Fitchner, 2010 – Sec. 11.3).

To our knowledge, the importance of the warping on the observed data $d(t + \Delta\tau)$ has been overlooked in the literature. Considering that the velocity model used in propagation still contains small kinematic errors, the warping to the modeled times means that the adjoint wavefield events will better correlate with the forward wavefield events. In practice, this better focuses the events in depth.

Once the FWI velocity model is generated at high frequencies, it is possible to convert this velocity into an image, which is comparable to the RTM or LSM products. Zhang et al. (2020) proposed to approximate the impedance contrasts by:

$$\frac{\partial I}{\partial n} \approx \rho \left(\frac{\partial v}{\partial x} sin\theta cos\varphi + \frac{\partial v}{\partial y} sin\theta sin\varphi + \frac{\partial v}{\partial z} cos\theta \right). \quad (3)$$

In this text, we will refer as FWI derived image to the application of Eq. (3) to the final FWI velocity model v. Often, the dominating term is $\frac{\partial v}{\partial z}$, which delivers a simple approximation for Eq. (3).

Gaussian Anomaly Example

Our first example is a synthetic model consisting of a half-space with a high velocity anomaly of Gaussian shape ($\Delta V = 150 \ m/s, L = 150m$) in the central part of the model, depicted in **Figure 1**. Synthetic seismograms were generated with a Ricker wavelet of 45Hz cut frequency and we used a towed-streamer regular acquisition with cable length of 3 km. Absorbing boundaries were imposed, so no multiples or ghosts were generated in this application.
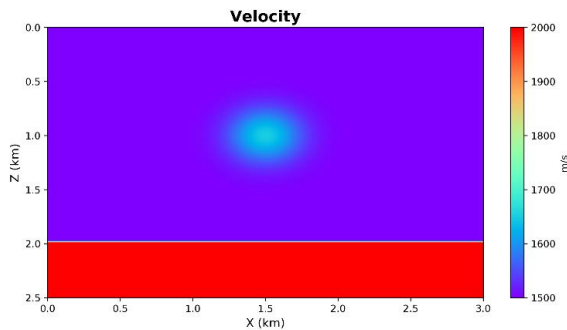

Figure 1: Gaussian anomaly model used to generate the synthetic data.

Once the dataset was generated, the models used for the RTM and FWI were a constant velocity model with $V = 1500 \ m/s$ (the same velocity of the upper half space of Figure 1). This means the propagation of the forward wavefield is realized in a kinematic incorrect model. We constrained the FWI updates, not allowing it to recover the Gaussian anomaly during the inversion.

The result of the application of RTM and the image derived from the FWI are depicted in **Figure 3** and **Figure 3**, respectively. Since the model used for migration has kinematic differences, we do not expect the right positioning and perfect focusing. Interesting enough the quality of the focusing in the FWI image is clearly superior to the RTM image. We emphasize that this application contains primaries only, no transmission losses and absent of illumination issues, since the acquisition consists of a perfectly regular geometry and with forward and reverse propagations within a constant velocity model. In this specific example and considering these constraints, we can discard the arguments that the improvement came

from the fact that FWI utilizes multiples events, compensates for transmission losses, and the iterative procedure correct for illumination issues.

What we can observe, however, in **Figure 4**, is that Eq. (2) imposes warping in the adjoint wavefield, increasing the time of the event at shorter offset. This is compatible with a constant velocity model that is absent of the high velocity anomaly used to generate the data. The consequence is that the FWI derived image (**Figure 3**), although not perfect, has much better focusing than the RTM image (**Figure 2**). The depth positioning of the FWI derived image is also not perfect (oscillations are clearly visible) and we do not expect to resolve this unless the propagating model is correctly retrieved. Still, this increase of focusing can be very helpful for interpretation in challenging scenarios.
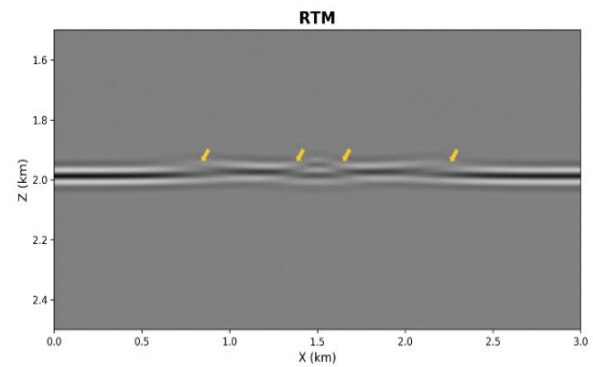

Figure 2: RTM image using input data from the Gaussian anomaly model but migrated with a constant velocity model. The yellow arrows point to defocused regions in the image.
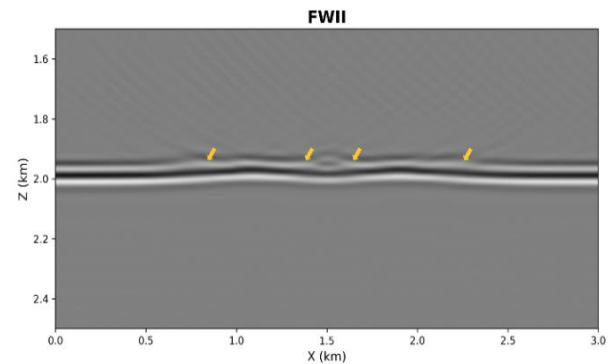

Figure 3: FWI image using input data from the Gaussian anomaly model but inverted with a constant velocity model in the upper half-space. The yellow arrows point to better focused regions in the image in comparison with **Figure 3.**
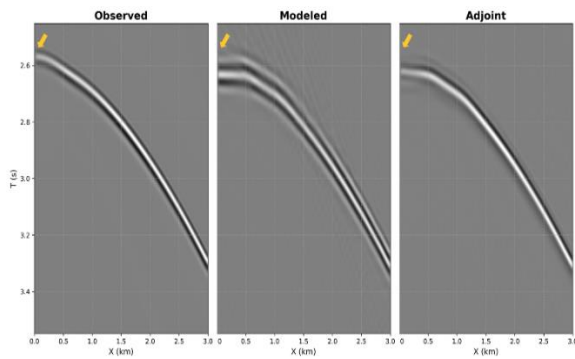
Figure 4: The observed data, $d(t)$, modeled data, $u(t)$, and the adjoint source, $\frac{\partial}{\partial t} d(t + \Delta \tau)$, for a seismogram at the central position of the model in **Figure 1**. Notice that there is a time shift at shorter offsets (pointed by the yellow arrow). The adjoint source is warped to the times of the modeled data.

Real Data Example

Our second example is a field data acquired by conventional towed streamers (narrow azimuth and 8.2 km cable length) of a 3D survey in Santos Basin, Brazil. Water depth in this region is about 2,200 m. In the preparation of this dataset, the multiples were removed using 3D SRME. The initial velocity model was obtained by standard tomography and interpretation of the salt body, after salt flood procedure. No tomographic procedure was applied in the salt or pre-salt section. The limited offset between source and receivers in the available towed streamer, the high velocities in the salt layer, and the large depth of the target hinder the FWI updates of low wavenumbers, which are needed at large depths. Despite the effort in improving the velocity model with this data, a longer offset and wide-azimuth acquisition would be more suitable for better updates.

In **Figure 5**, we compare the images generated by RTM using the initial and the final models from the FWI flow and the image derived from the FWI velocity model. These images are limited to 30Hz cut frequency. It's worth mentioning that all three results are the raw output of each corresponding algorithm, with no post-processing or regularization schemes used in this application.

The first remarking fact is that we observe differences in positioning and focusing between the RTM with different velocity models, but the migration artifacts are strongly present in both RTM images. The FWI derived image is positioned at the same depths as the RTM with the final FWI velocity, but the events are more continuous, the faults are better imaged, and stratigraphic details are better resolved. Since the multiples were attenuated in this dataset, we mainly attribute this improvement to the time shift correction in the FWI adjoint source.

Discussion

One might wonder if we could go straight to the high frequencies and apply the warping procedure in a least-squares migration procedure. Our experience indicates

that the multiscale approach in frequency is important to guarantee the best results. The low frequency updates in the velocity generate the indication of where the reflectors should be imaged, and this is important for the higher band of frequencies. Going straight to the high frequencies tend to generate results similar to the RTM results of **Figure 5**.

Conclusions

The increase of computational capacity and the development of robust schemes enable innovative methods for imaging based on FWI methods. This work brings a new argument, with two examples, to explain the improvement seen in the final image, when compared with traditional RTM image. We believe that the time shift correction in the FWI adjoint source plays an important role for the image focusing, in the presence of remaining kinematic issues in the velocity model. We hope that future experience gained from practical applications will help the understanding of this novel technology.

Acknowledgments

References

Biondi, B., Almomin, A., 2013, Tomographic full-waveform inversion (TFWI) by combining FWI and wave-equation migration velocity analysis: The Leading Edge (2013),**32**(9): 1074, doi:10.1190/tle32091074.1.

Claerbout, J. F., 1985, Imaging the Earth's Interior: Blackwell Science Inc.

Fitchner, A. 2010, Full Seismic Waveform Modelling and Inversion: Springer, Berlin, Heidelberg.

Huang, R., Z. Zhang, Z. Wu, Z. Wei, J. Mei, and P. Wang, 2021, Full-waveform inversion for full-wavefield imaging: Decades in the making: The Leading Edge, **40**, no. 5, 324–334, doi:10.1190/tle40050324.1.

Luo, Y., and G. T. Schuster, 1991, Wave-equation traveltime inversion: Geophysics, **56**, 545–653, doi:10.1190/1.1443081.

Ma, Y., Hale, D., 2013: Wave-equation reflection traveltime inversion with dynamic warping and full-waveform inversion, Geophysics **78** (6):223-233, doi:10.1190/geo2013-0004.1

Métivier, L., Allain, A., Brossier, R., Mérigot, Q., Edouard Oudet, E., and Virieux, J., 2018, Optimal transport for mitigating cycle skipping in full-waveform inversion: A graph-space transform approach, Geophysics **83**: R515-R540. doi:10.1190/geo2017-0807.1

Vigh, D., X. Cheng, K. Jiao, Z. Xu, and W. Dai, 2019, Is the salt-related full-waveform inversion sorted out?: 89th

Annual International Meeting, SEG, Expanded Abstracts, 1265–1269, doi:10.1190/segam2019-3215741.1

Wei, Z., J. Mei, Z. Wu, Z. Zhang, R. Huang, and P. Wang, 2021, Unlocking unprecedented seismic resolution with FWI imaging: 82nd Annual Conference & Exhibition, EAGE, Extended Abstracts, doi:10.3997/2214-4609.202113217

Warner, M., and L. Guasch, 2014: Adaptive waveform inversion: 84th Annual International Meeting, SEG,

Expanded Abstracts, 1089–1093, doi:10.1190/segam2014-0371.1.

Zhang, Z.; Wu, Z. Wu; Wei, Z.; Mei, J.; Huang, R.; Wang, P., 2020, FWI Imaging: Full-wavefield imaging through full-waveform inversion: SEG Technical Program Expanded Abstracts: 656-660. doi:10.1190/segam2020-3427858.1

Zhang, Z., Wu, Z., Wei, Z., Mei, J., Huang, R., Wang, P., 2023, Enhancing salt model resolution and subsalt imaging with elastic FWI: The Leading Edge **42**: 207–215. doi:10.1190/tle42030207.1
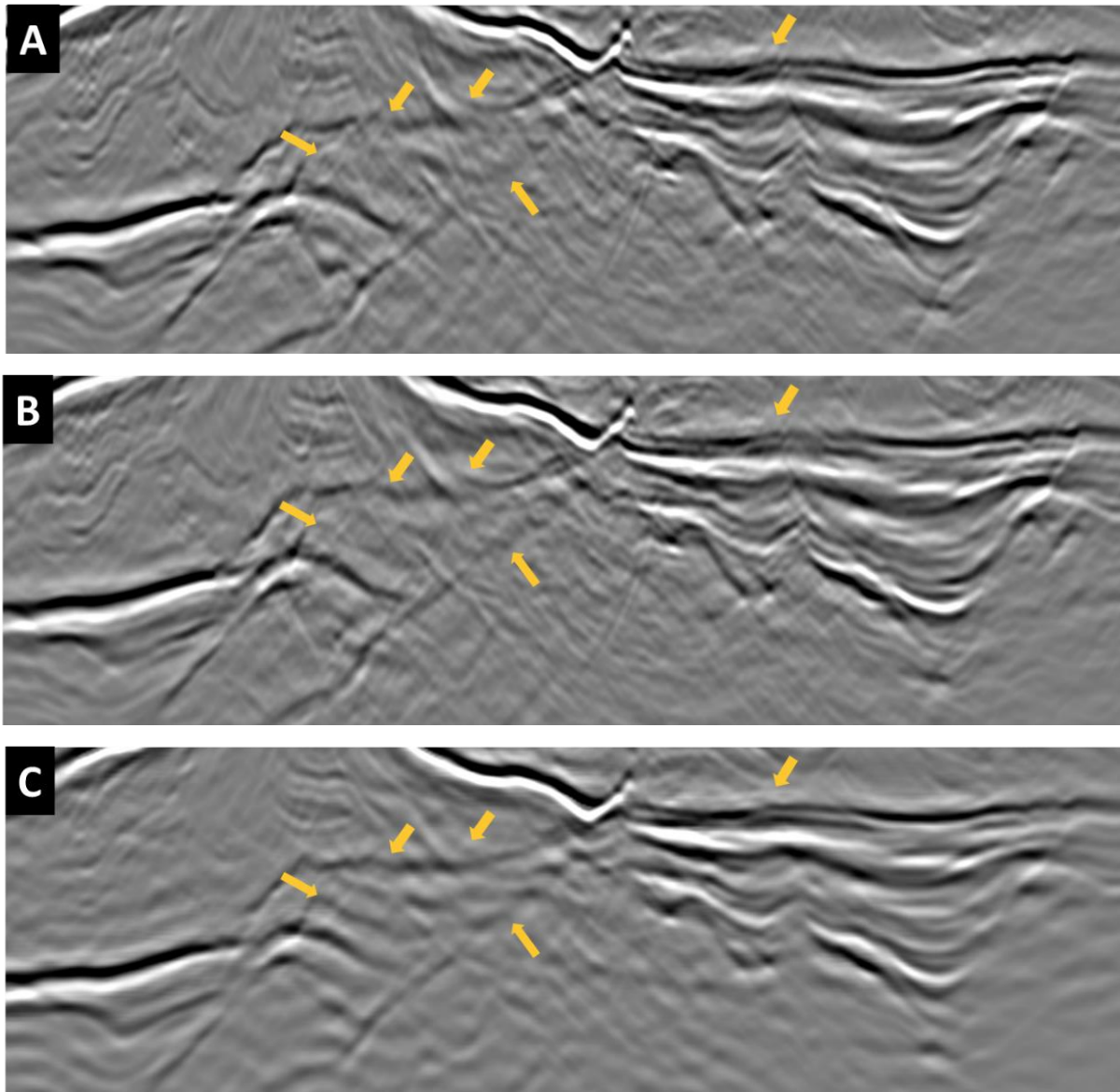

Figure 5: (A) RTM image using the initial velocity model, (B) RTM image using the final FWI velocity model, and (C) FWI derived image. Although, it is possible to see mild improvements from (A) to (B), the FWI derived image (C) has much better event continuity and less migration artifacts (pointed by yellow arrows).